Wavefront shaping and imaging through a multimode hollow-core fiber

ZHOUPING LYU[1,2,*] AND LYUBOV V. AMITONOVA[1,2]

[1]*Advanced Research Center for Nanolithography (ARCNL), Science Park 106, 1098 XG Amsterdam, The Netherlands*
[2]*Department of Physics and Astronomy, Vrije Universiteit Amsterdam, De Boelelaan 1105, 1081 HV Amsterdam, The Netherlands*
*z.lyu@arcnl.nl

Abstract: Multimode fibers recently emerged as compact minimally-invasive probes for high-resolution deep-tissue imaging. However, the commonly used silica fibers have a relatively low numerical aperture (NA) limiting the spatial resolution of a probe. On top of that, light propagation within the solid core generates auto-fluorescence and Raman background, which interferes with imaging. Here we propose to use a hollow-core fiber to solve these problems. We experimentally demonstrate spatial wavefront shaping at the multimode hollow-core fiber output with tunable high-NA. We demonstrate raster-scan and speckle-based compressive imaging through a multimode hollow-core fiber.

1. Introduction

Multimode fibers (MMFs) enable high-resolution *in vivo* imaging due to their inherent flexibility, simplicity, and minimal sample damage [1–5]. The ultimate goal of MMF-based imaging is to provide high-resolution high-contrast imaging through a compact sensor with a minimized footprint. Two common methods of imaging through an MMF are raster-scan (RS) imaging and compressive imaging (CI). RS imaging relies on wavefront shaping (WFS) and optimized focal spots that are scanned across the sample, while CI uses random speckle illumination and computational reconstruction [6–12]. A conventional MMF usually consists of a silica core and a doped silica cladding. The pump laser produces Raman scattering while propagating through a fiber core [13,14]. The laser beam also interacts with residual photoactive compounds of an optical fiber, leading to auto-fluorescence signal [15]. Therefore, Raman and auto-fluorescence signals of fused silica accumulated during light propagation through a fiber probe provide a strong background and decrease measurement sensitivity. Scattering and reflection at the interfaces of an MMF further increase the unwanted background signal. Spectral filtering can help to partially reduce the background, but it also attenuates the fluorescent signal from the sample. The low signal-to-background ratio reduces the imaging contract and may totally destroy the fiber-based imaging of weak fluorescent samples.

Recently, hollow-core fibers (HCFs) have attracted a lot of interest [16,17]. A hollow air-filled core offers unique properties for a wide range of applications: from gas laser and pulse compression to sensing, communication, and imaging [18–22]. The image reconstruction through an HCF via deep learning has been demonstrated [23]. The small overlap between the guided light and the solid cladding material provides low auto-fluorescence and Raman background signal in comparison with standard fused silica waveguides [24–26]. The dispersion of the HCF is relatively low because of the absence of material dispersion [17]. HCFs can substantially improve the signal collection efficiency in nonlinear optical fiber endoscopy and have been shown to enable high-sensitive detection of the Raman signal [26–28].

A hollow waveguide with internal metallic coatings is an attractive candidate among different categories of HCF [29]. Unlike other HCFs, such as hollow-core photonic bandgap fibers and antiresonant HCFs, which are designed to guide a limited number of low-order modes resulting in a numerical aperture (NA) of less than 0.05, an internal metallic hollow waveguide allows a continuum of modes to propagate, each with different attenuation coefficient [16,30]. In geometric ray optics, light propagating through an internal metallic hollow waveguide reflects off the dielectric film. Lower-order modes reflect fewer times, while higher-order modes reflect more frequently, leading to faster attenuation of the higher-order modes. Therefore, the internal metallic HCF can offer a high-NA that depends on the fiber length and diameter.

Here we experimentally demonstrate the wavefront shaping through multimode hollow-core fibers (MHCFs). We generate and investigate diffraction-limited foci with an NA higher than 0.4 at the MHCF output. Furthermore, we experimentally demonstrate high-resolution imaging through the MHCF by two approaches: RS imaging with optimized illumination and CI with random speckle illumination.

2. Methods

2.1. Experimental setup

Figure 1(a) shows the experimental setup. We use bare MHCFs, which are hollow silica tubes with a highly reflective silver (Ag) coating deposited on the inner surface. The fibers have a length of 7 cm and core diameters of 500 and 300 μm (Guiding Photonics). The cross-section of the MHCF probe is shown in Fig. 1(b). The mode profiles of the internal metallic MHCF are similar to that of a step-index MMF and can be determined by solving Maxwell's equations with the appropriate cylindrical boundary conditions [31]. However, the propagation constants of modes in MHCFs are complex numbers, indicating that all modes are leaky. In theory, the attenuation constant α, can be estimated as $\alpha = 0.5 n_0 k_0 d^2 (1 - R) U$, where U is the transverse phase constant, R is the reflection coefficient, d is fiber diameter, k_0 is the wavevector, and $n_0 = 1$ is the refractive index of the core [29,32]. High-order modes, with larger U and smaller R, have higher transmission losses. Thus the NA and losses depend on the fiber length, fiber diameter, and the NA of the input coupling objective.

We use a continuous-wave light source with a wavelength of 532 nm [Cobolt Samba] as a pump and expand it to a beam diameter of 8 mm. After being reflected by a mirror (M1), the laser beam is incident to the Digital Micromirror Device (DMD) from Texas Instrument driven by the DLP V-9501 VIS module (Vialux). The −1st diffraction order of the DMD passes through the pinhole (P1), and the phase modulation of the DMD is imaged at the pupil plane of the input objective (Obj1) by the 4f system consisting of two lenses, L1 (f1 = 150 mm) and L2 (f2 = 100 mm). Throughout the experiments, we used three different input objectives to investigate the NA of the MHCF:

- Olympus RMS10X: 10×, NA = 0.25;

- Olympus RMS20X: 20×, NA = 0.4;

- Olympus RMS20X-PF: 20×, NA = 0.5.

The output of the MHCF is imaged on Camera1 by an output objective (Obj2, Leica, 63x, NA = 0.7) and a tube lens (L4, f4 = 250 mm). A sample is put at the output plane of the MHCF. The fluorescent signal from the sample is collected by the same MHCF, separated from the pump beam by a dichroic mirror (DM), and recorded by an avalanche photodiode detector (APD, Thorlabs) with a lens (L5, f5 = 60 mm). A notch filter (NF) is used to further remove the input light from the fluorescence signal.

(a)

(b)

(c)
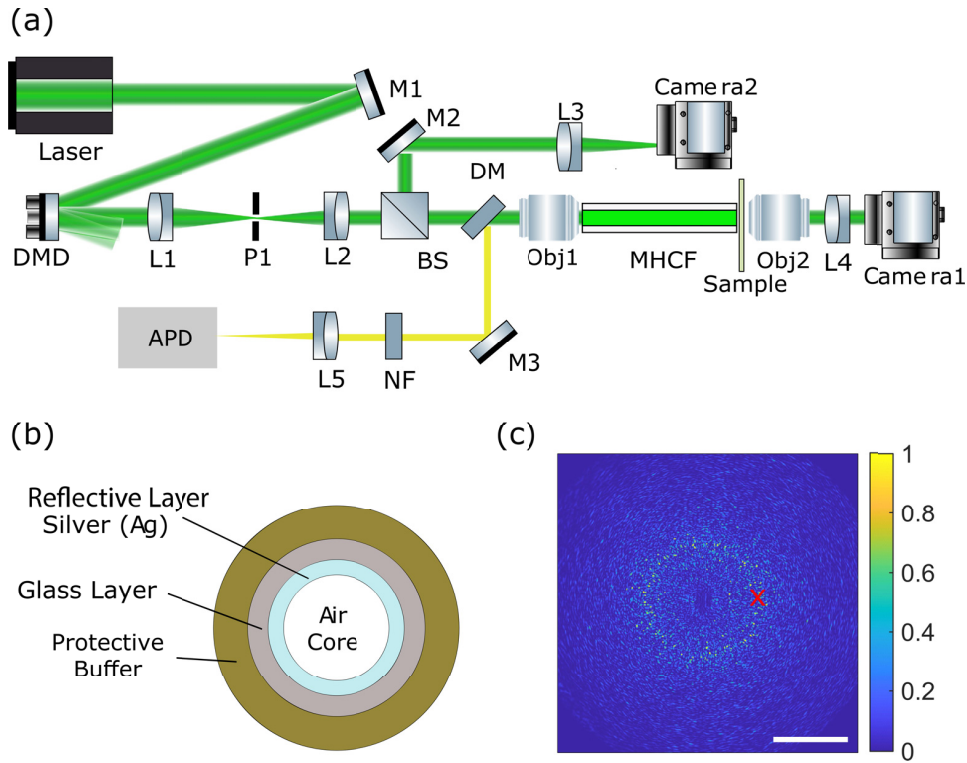
Fig. 1. (a) Schematic of the experimental setup. DMD, Digital Micromirror Device; L, lens; P, pinhole; M, mirror; BS, beam splitter; DM, dichroic mirror; Obj, Objective; NF, notch filter; APD, avalanche photodiode detector. (b) The cross-section of the multimode hollow-core fiber (MHCF). (c) Speckle pattern at the output of the MHCF when the input light is focused at the location marked by the red cross. Core diameter is 500 μm. The scale bar is 100 μm.

2.2. Spatial wavefront shaping

Similar to a step-index MMF, coherent light coupled into an MHCF is decomposed into fiber modes. The output can be calculated as the sum of all these propagated, weighted, leaky modes, which results in a speckle pattern. Figure 1(c) shows the output of the MHCF with a core diameter of 500 μm. The light is coupled to the MHCF at the input facet position marked by the red cross, using an Olympus RMS10X objective with an NA of 0.25. The bright ring structure with higher intensity is observed at the same radial position as the input light. A DMD has been used for spatial WFS. A DMD chip contains thousands of micromirrors arranged in a grid, each capable of rotating ±12° to switch between 'on' and 'off' states. Arranging the 'on' and 'off' state of the micromirrors as a grating. Lee hologram encodes the relative phase shift to the spatial shift between the adjacent gratings [33]. Compared with the liquid crystal SLMs, DMDs give a higher beam shaping fidelity with a faster modulation rate [34]. The optimized wavefronts are calculated by a feedback-based algorithm and then projected onto the DMD, creating the targeted light distributions on the fiber output [6].

We use the dual reference algorithm to create a focal spot at the MHCF output facet [35]. The DMD segments are divided into two equal groups, Group 1 and Group 2, each containing 1024 segments. To create an overlapping area, 60 central segments are shared between both groups. In the first step, we use Group 2 segments as a reference and sequentially project 1024 Hadamard

patterns onto Group 1 segments. For each Hadamard pattern, the relative phase between the two groups is changed from 0 to 2π in 3 steps by varying the phase of Group 2 as $[0, 2/3\pi, 4/3\pi]$. For each combination of the Hadamard basis pattern on Group 1 segments and the phase setting on Group 2 segments, we measure the intensity at the target using the camera. Then the optimized phase pattern for Group 1 for each focus position on the fiber output is calculated based on the Fourier transform and the Hadamard transform. In the second step, we reverse the roles and use Group 1 as the reference. We project the Hadamard basis patterns onto Group 2 segments and follow the same procedure: varying the phase of Group 1 while measuring the corresponding intensity at the target. The overlapping area between Group 1 and Group 2 is utilized to determine the relative phase difference between the two groups. Finally, the global optimized phase pattern to focus the light into a focal spot at the MHCF output is calculated. In our experiment, we therefore have 1988 effective DMD segments, 6144 phase patterns projected to the DMD, and 6144 images acquired by the camera. The camera has a limited frame rate of up to 100 Hz. Therefore, pre-calibration requires around 1 minute for data collection. In the next step, these optimized wavefronts are projected to the DMD one by one to create the foci at the output of the MHCF.

2.3. Imaging through a hollow-core fiber

We experimentally implement two modalities of computational imaging through an MHCF: WFS-based RS imaging and random speckle-based CI. For RS imaging, we use an optimized wavefront at the input facet of the MHCF to create a focal spot at the sample plane. As only one sample point is illuminated at a time, 2D imaging requires scanning over a regular raster, which is performed by projecting a set of optimized patterns on the DMD. Thus, a sequential scan of the optimized foci at a sample plane is performed in a zigzag pattern within a square frame. For each focal spot illumination, the fluorescent signal from the sample is collected by the same MHCF, filtered out by the DM, and then detected by the APD. Imaging of an unknown sample (consisting of $N \times N$ pixels) with a single-pixel detection scheme can be generally described as a linear matrix equation:

$$Ax = y, \tag{1}$$

where A is the measurement matrix ($M \times N^2$) constructed from the flattened illumination patterns, y is a $M \times 1$ vector consisting of the total measured signal for each illumination, and x is $N^2 \times 1$ vector representing the flattened unknown sample. In the case of RS imaging with $M = N^2$ optimized foci on the MHCF output, A can be approximated by a square $N^2 \times N^2$ eye matrix leading to $x = y$. As a result, one can get the 2D image by simply reshaping y to a 2D $N \times N$ matrix.

In contrast to RS imaging, CI employs a 2D zigzag scanning at the input facet of the MHCF, creating a series of random speckle patterns on the sample placed at the fiber output. The M speckle patterns are recorded as images of $N \times N$ pixels during the pre-calibration step, using Camera1. These patterns are transformed into M row vectors with a size of $1 \times N^2$. By stacking the row vectors, we form an $M \times N^2$ measurement matrix A. The total fluorescence response for every illumination pattern is collected by the same fiber and measured with an avalanche photodiode in the same way as in RS imaging, resulting in $M \times 1$ signal vector y

The CI process can be also described using Eq. (1) The main difference from RS is that the measurement matrix, A, is rectangular with the number of rows much smaller than the number of columns, $M \ll N^2$. Compressive sensing algorithms enable the solution of this underdetermined system of linear equations with two main conditions. First, the measurement matrix A must be incoherent, which ensures uniform sampling of the data. Second, the sample should be sparse in a certain domain, such as the spatial sparsity and the total variation (TV) sparsity. The spatial sparsity implies that only a few elements of sample vector x are nonzero, which is commonly quantified by the ℓ_0-norm. Since ℓ_0-norm minimization is NP-hard, ℓ_1-norm minimization is

often used as a computationally feasible approximation [36]. The `TV` sparsity is quantified by $\sum_i \|D_i x\|_2$, where $D_i x$ represents the discrete gradient of x at pixel i and $\|\cdot\|_2$ is l_2-norm. The TV minimization problem involves minimizing this quantity, and various particular algorithms, such as `tveq`, `tvqc`, and `tval3` are used [36–38]. These algorithms differ in their constraints and optimization procedures. We choose the total variation `TV` minimization `tval3`, which uses the gradient sparse prior information with equality constraints. Specifically, we use the isotropic denoising model: $\min_x \sum_i \|D_i x\|_2$, subject to $Ax = y, x \geq 0$. TV algorithm's gradient sparse assumption provides sharp edges and smooth fields, and `tval3` offers relatively faster performance compared to other TV minimization algorithms.

3. Results

In the first set of experiments, we demonstrate WFS through the MHCF. We use a hollow fiber with a core diameter of 500 μm and the coupling microscope objective Olympus RMS10X with NA of 0.25. Multiple foci at different locations arranged in a 10×10 grid have been optimized around the center of the MHCF using a single WFS procedure described above. The distance between two optimized focal spots on the MHCF output is 5.3 μm. The incoherent sum of the foci within a field of view of 55.8 μm by 55.8 μm is presented in Fig. 2(a). WFS allows us to precisely control the light on the output of hollow fiber.

In the second set of experiments, we compare the performance of WFS through the same MHCF for different coupling NAs. We investigate the NA range from 0.25 to 0.5. We repeat the experiments for three input objectives as described in the experimental setup section to experimentally change the input NA. The results are presented in Fig. 2. The focal spots have been optimized at the same positions on the output fiber facet. The incoherent sum of all the foci for the input objectives with NA of 0.25, 0.4, and 0.5 are shown in Fig. 2(a). We can see that the higher input NA leads to a smaller size of focal spots after the WFS procedure.

For quantitative analysis, each generated focal spot is fitted with a 2D Gaussian function, allowing us to calculate the width of a focal spot along the short axis ($2w_{\min}$) and the long axis ($2w_{\max}$) at half-maximum. The focus shape is characterized by the ellipticity $\varepsilon = 1 - w_{\min}/w_{\max}$ and the orientation of the long main axis. The power in the focal spot is characterized by a power ratio PR $= I_{\text{foc}}/I_{\text{tot}}$, where I_{tot} represents the total power within the whole field of view (55.8 μm by 55.8 μm) and I_{foc} is the power within the fitted 2D Gaussian function at or above the half-maximum level. The ellipticity of the foci generated at the output of a MHCF for the input objectives with NA of 0.25, 0.4, and 0.5 are shown in Fig. 2(b) where darker green colors correspond to more rounded shapes (lower ellipticity) and brighter green colors indicate higher ellipticity. The directions of the long axes of the foci are indicated by the white lines. The long main axis tends to align with the azimuthal direction as could be expected from the spatial distributions of the guided modes. However, for many foci, the direction appears chaotic. The PR of the foci generated by WFS are presented in Fig. 2(c) for the input objectives' NA of 0.25 (left), 0.4 (middle), and 0.5 (right). The foci are less elliptical with higher PR for WFS with a lower NA objective, which is expected as the lower the NA, the lower the ratio between the number of modes and the number of DMD segments, resulting in more effective WFS.

We characterize the NA of the generated foci for different input objectives by analyzing their full width at half maximum (FWHM). The FWHM of the short axis, $2w_{\min}$, for different focal spots is extracted by independently fitting each focal spot by a 2D tilted Gaussian function. The NA is then calculated assuming diffraction-limited foci as $\text{NA}_f = \lambda/(4w_{\min})$, where λ is the wavelength of the input light. The averaged NA of 100 foci on the MHCF output generated by WFS for 3 different input objectives are presented in the second column of Table 1. We also calculate the NA of speckles within the same field of view of 55.8 μm by 55.8 μm. We couple light to the MHCF using different objectives and different input beam positions and record speckle patterns on the fiber output. The averaged two-dimensional (2D) spatial power spectrum
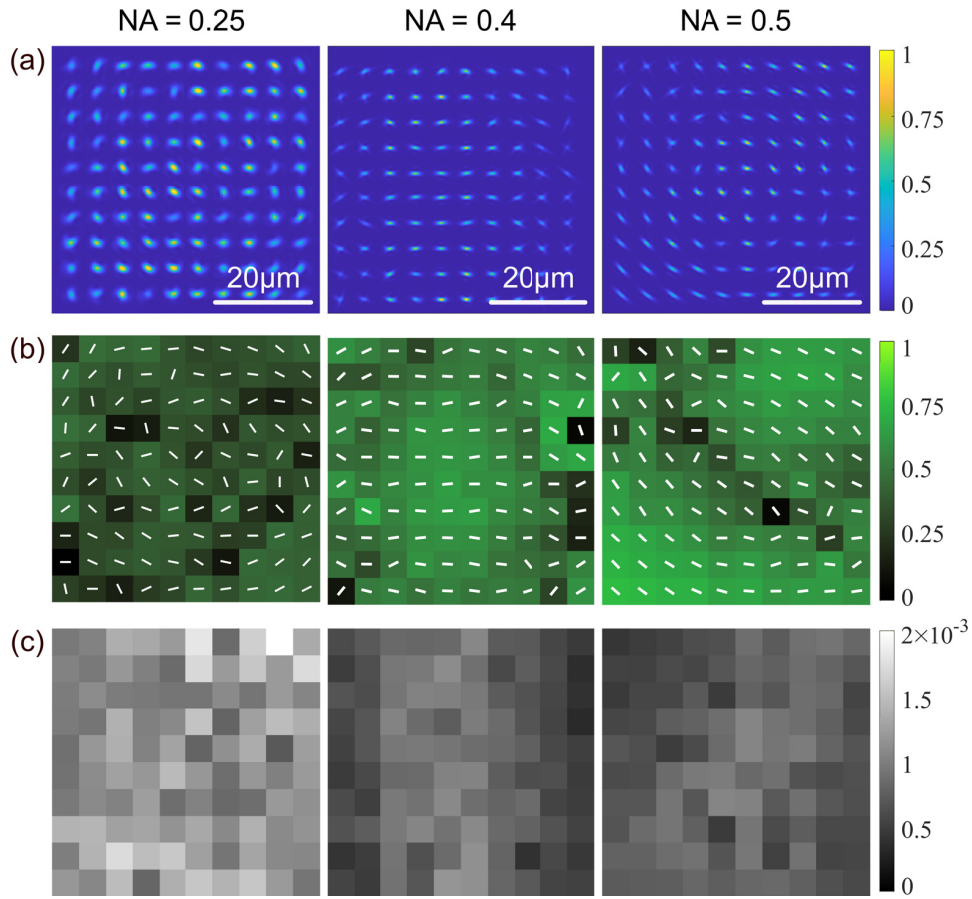
Fig. 2. Wavefront shaping through a hollow fiber with a core diameter of 500 μm. (a) The incoherent sum of independently generated focal spots at the MHCF output arranged in a 10×10 grid around the center using input objectives with different NA: 0.25 (left), 0.4 (middle), and 0.5 (right). The presented field of view is 55.8 μm by 55.8 μm. The scale bars are 20 μm. (b)-(c) Characterization of the focal spots quality. (b) The ellipticity $\varepsilon = 1 - w_{min}/w_{max}$ of each focal spot. Dark green colors correspond to more rounded shapes (lower ellipticity) while bright green colors indicate higher ellipticity. The orientations of the long main axes are presented by the white lines. (c) The power ratio calculated as the power within the focal spot at the full-width at half maximum level with respect to total power within the field of view.

for each objective is calculated by averaging the 2D fast Fourier transform of 900 speckle patterns generated with the given objective. The cutoff frequency of the averaged spatial power spectrum, ν_{cutoff}, is identified at the point where the slope of the curve's descent noticeably decreases. The NA is then calculated by $\nu_{cutoff} = 2NA_f/\lambda$. The estimated NAs of speckle patterns for different input NAs are presented in the third column of Table 1. The calculated NA for the hollow fiber output derived from speckle patterns and optimized foci match very well, confirming the accuracy of the measurements. For the first two input objectives with NA of 0.25 and 0.4, the calculated NA of the hollow fiber output is close to the NA of the objective. However, for the input objective with an NA of 0.5, the estimated NA is noticeably lower. This can be explained by more rapid attenuation of higher-order modes within a hollow fiber.

Table 1. The experimentally estimated NAs of WFS-based foci and speckles for three objectives with different input NAs.

| Input NA	Foci	Speckles
0.25	0.22	0.23
0.4	0.39	0.37
0.5	0.41	0.42

In the final set of experiments, we demonstrate the potential of an MHCF to serve as a high-NA imaging probe. We experimentally demonstrate RS imaging and CI through a hollow fiber. We use an MHCF with a diameter of 300 μm and the input objective with an NA of 0.4 and a pupil plane diameter of 7.2 mm (Olympus RMS20X). As a sample, we use a fluorescent microparticle (PS-FluoRed-1.0) with a diameter of 1.14 μm. As a reference, the bright-field image of the sample is captured using an objective with NA of 0.7 and Camera1. The result is presented in Fig. 3(a). For the RS imaging, a 40×40 foci arranged in a grid with a distance of 0.175 μm is optimized using WFS as described above. The distance between the optimized foci is chosen to be small enough to provide high-quality diffraction-limited imaging. Each focal spot is sequentially projected on the fiber output and used to illuminate the sample at a certain location. As a result, we can scan illumination across the sample. The result of RS imaging is presented in Fig. 3(c). The measurement speed of RS imaging is limited by the DMD fresh rate, which is up to 23 kHz and can reach 14 frames per second with 40×40 focal spots per frame.

To demonstrate CI through an MHCF, we use a set of 900 speckle patterns generated at the output facet of an MHCF. During the pre-calibration step, we record the intensity distribution of every speckle pattern with the camera. Then the speckles are cropped to the desired field of view of 7.2 $\mu m \times 7.2$ μm at the center of the MHCF and resized to 33×33 pixels. The low coherence of speckle patterns is one of the main preconditions for compressive imaging. Therefore, we characterize the correlation of the 900 speckle patterns using the cross-correlation coefficient γ, calculated between every pair of patterns as:

$$\gamma = \frac{\sum_i \sum_j (S_{ij} - \bar{S})(P_{ij} - \bar{P})}{\sqrt{\sum_i \sum_j (S_{ij} - \bar{S})^2 \sum_i \sum_j (P_{ij} - \bar{P})^2}}, \tag{2}$$

where S_{ij} and P_{ij} denote the pixel values of experimentally measured speckle illumination patterns S and P at position (i, j), respectively. $\bar{S}$ and $\bar{P}$ represent the mean pixel values of speckle patterns S and P. The results are presented in Fig. 3(b), which displays a matrix of correlation coefficients, where each element γ_{ij} represents the correlation between the i-th and j-th speckle patterns. The diagonal of the matrix, where each speckle pattern is compared with itself, exhibits maximum correlation, while off-diagonal elements show relatively low correlations between different speckle patterns. The average value of γ for non-diagonal elements is 0.08, which proves the low coherence between speckles of an MHCF.

During the imaging step, we sequentially illuminate the sample with the same set of 900 patterns. The total fluorescence response for every illumination pattern is collected by the same fiber and measured with an avalanche photodiode, resulting in $M \times 1$ signal vector $\mathbf{y}$. The total variation TV minimization `tval3` algorithm is used to solve Eq. (1) and reconstruct the image. The result of CI is shown in Fig. 3(d). With the same DMD fresh rate, CI can potentially achieve a video rate of 25 frames per second.
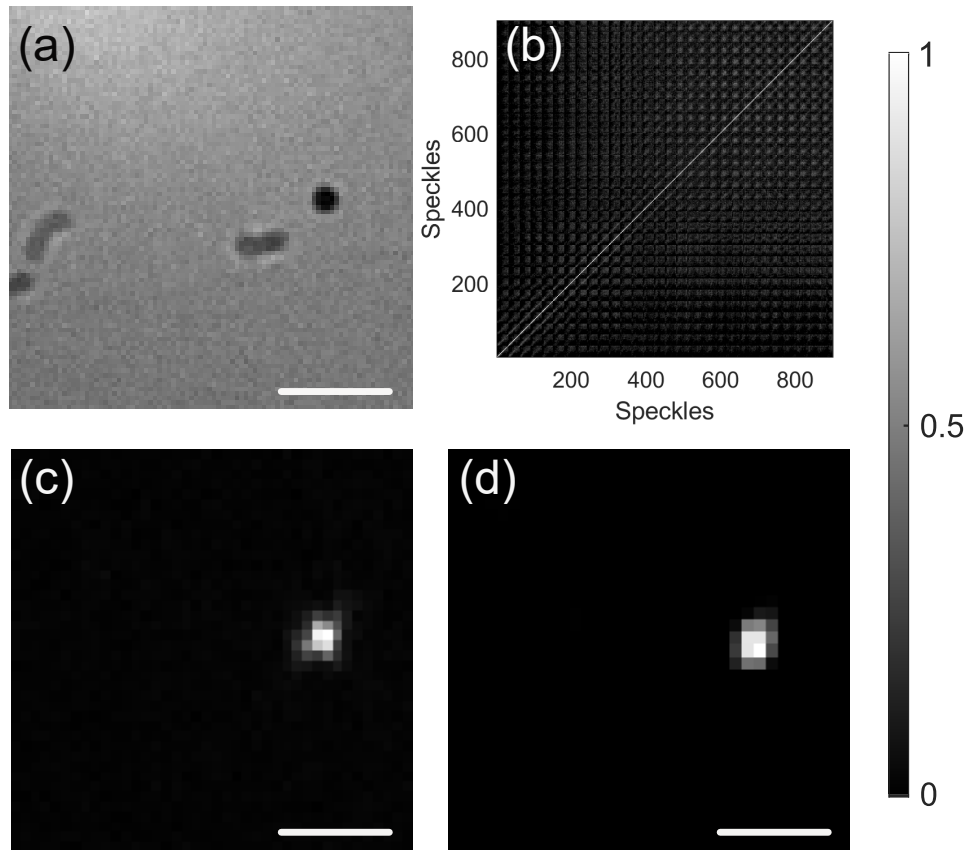
Fig. 3. (a) Bright-field reference image of 1.14 μm fluorescent bead. (b) A matrix of correlation coefficients, γ, of 900 speckle illumination patterns used for CI. The color intensity indicates the degree of correlation, with lighter colors representing higher correlations and darker colors indicating lower correlations. (c)-(d) Experimentally acquired images of the sample through an MHCF probe by RS imaging (c) and CI approach (d). The scale bars are 2 μm.

4. Conclusion

We experimentally demonstrated spatial WFS through an MHCF. We investigated the NA of MHCF-based imaging for different input objectives. We demonstrate that the NA on the output of an MHCF can be more than 0.4 for an MHCF with a diameter of 500 μm and a length of 7 mm. We successfully performed the proof-of-concept experiments demonstrating raster-scan imaging and compressive imaging through an MHCF for a simple single fluorescent bead sample. Our results show the potential of MHCF being a high-NA low background imaging probe.

Data availability. Data underlying the results presented in this paper are not publicly available at this time but may be obtained from the authors upon reasonable request.

References

1. H. Cao, T. Čižmár, S. Turtaev, *et al.*, "Controlling light propagation in multimode fibers for imaging, spectroscopy, and beyond," Adv. Opt. Photonics **15**(2), 524–612 (2023).
2. S. A. Vasquez-Lopez, R. Turcotte, V. Koren, *et al.*, "Subcellular spatial resolution achieved for deep-brain imaging in vivo using a minimally invasive multimode fiber," Light: Sci. Appl. **7**(1), 110 (2018).
3. S. Turtaev, I. T. Leite, T. Altwegg-Boussac, *et al.*, "High-fidelity multimode fibre-based endoscopy for deep brain in vivo imaging," Light: Sci. Appl. **7**(1), 92 (2018).
4. S. Ohayon, A. Caravaca-Aguirre, R. Piestun, *et al.*, "Minimally invasive multimode optical fiber microendoscope for deep brain fluorescence imaging," Biomed. Opt. Express **9**(4), 1492–1509 (2018).
5. Z. Wen, Z. Dong, Q. Deng, *et al.*, "Single multimode fibre for in vivo light-field-encoded endoscopic imaging," Nat. Photonics **17**(8), 679–687 (2023).
6. I. M. Vellekoop and A. Mosk, "Focusing coherent light through opaque strongly scattering media," Opt. Lett. **32**(16), 2309–2311 (2007).
7. T. Čižmár and K. Dholakia, "Exploiting multimode waveguides for pure fibre-based imaging," Nat. Commun. **3**(1), 1027 (2012).
8. I. T. Leite, S. Turtaev, D. E. Boonzajer Flaes, *et al.*, "Observing distant objects with a multimode fiber-based holographic endoscope," APL Photonics **6**(3), 036112 (2021).
9. O. Katz, Y. Bromberg, and Y. Silberberg, "Compressive ghost imaging," Appl. Phys. Lett. **95**(13), 131110 (2009).
10. M. Pascucci, S. Ganesan, A. Tripathi, *et al.*, "Compressive three-dimensional super-resolution microscopy with speckle-saturated fluorescence excitation," Nat. Commun. **10**(1), 1327 (2019).
11. L. V. Amitonova and J. F. de Boer, "Endo-microscopy beyond the abbe and nyquist limits," Light: Sci. Appl. **9**(1), 81 (2020).
12. B. Lochocki, A. Ivanina, A. Bandhoe, *et al.*, "Swept-source multimode fiber imaging," Sci. Rep. **13**(1), 8071 (2023).
13. D. Wardle, "Raman scattering in optical fibres," Ph.D. thesis, ResearchSpace@ Auckland (1999).
14. R. H. Stolen, "Nonlinearity in fiber transmission," Proc. IEEE **68**(10), 1232–1236 (1980).
15. M. Bianco, A. Balena, M. Pisanello, *et al.*, "Comparative study of autofluorescence in flat and tapered optical fibers towards application in depth-resolved fluorescence lifetime photometry in brain tissue," Biomed. Opt. Express **12**(2), 993–1009 (2021).
16. M. Komanec, D. Dousek, D. Suslov, *et al.*, "Hollow-core optical fibers," Radioengineering **29**(3), 417–430 (2020).
17. E. N. Fokoua, S. A. Mousavi, G. T. Jasion, *et al.*, "Loss in hollow-core optical fibers: mechanisms, scaling rules, and limits," Adv. Opt. Photonics **15**(1), 1–85 (2023).
18. T. Balciunas, C. Fourcade-Dutin, G. Fan, *et al.*, "A strong-field driver in the single-cycle regime based on self-compression in a kagome fibre," Nat. Commun. **6**(1), 6117 (2015).
19. M. R. A. Hassan, F. Yu, W. J. Wadsworth, *et al.*, "Cavity-based mid-ir fiber gas laser pumped by a diode laser," Optica **3**(3), 218–221 (2016).
20. Z. Yang, W. Yuan, and C. Yu, "Hollow core bragg fiber-based sensor for simultaneous measurement of curvature and temperature," Sensors **21**(23), 7956 (2021).
21. X. Wang, D. Ge, W. Ding, *et al.*, "Hollow-core conjoined-tube fiber for penalty-free data transmission under offset launch conditions," Opt. Lett. **44**(9), 2145–2148 (2019).
22. A. Lombardini, V. Mytskaniuk, S. Sivankutty, *et al.*, "High-resolution multimodal flexible coherent raman endoscope," Light: Sci. Appl. **7**(1), 10 (2018).
23. Y. Huang, K. Zhang, Z. Chen, *et al.*, "Image reconstruction through a hollow core fiber via deep learning," Opt. Commun. **488**, 126840 (2021).
24. S. Luan, S. Chen, X. Zhu, *et al.*, "In-situ background-free raman probe using double-cladding anti-resonant hollow-core fibers," Biomed. Opt. Express **15**(3), 1709–1718 (2024).
25. F. Yu and J. Knight, "Negative curvature hollow core optical fiber," IEEE J. Sel. Top. Quantum Electron. **22**(2), 146–155 (2016).
26. S. Yerolatsitis, F. Yu, S. McAughtrie, *et al.*, "Ultra-low background raman sensing using a negative-curvature fibre and no distal optics," J. Biophotonics **12**(3), e201800239 (2019).
27. A. Klioutchnikov, D. J. Wallace, M. H. Frosz, *et al.*, "Three-photon head-mounted microscope for imaging deep cortical layers in freely moving rats," Nat. Methods **17**(5), 509–513 (2020).
28. L. V. Doronina-Amitonova, V. F. Il'ya, A. B. Fedotov, *et al.*, "Raman detection of cell proliferation probes with antiresonance-guiding hollow fibers," Opt. Lett. **37**(22), 4642–4644 (2012).
29. H. Jelínková, M. Němec, J. Šulc, *et al.*, "Hollow waveguide delivery systems for laser technological application," Prog. Quantum Electron. **28**(3-4), 145–164 (2004).
30. M. Szwaj, I. A. Davidson, P. B. Johnson, *et al.*, "Double-clad antiresonant hollow-core fiber and its comparison with other fibers for multiphoton micro-endoscopy," Sensors **24**(8), 2482 (2024).
31. E. A. J. Marcatili and R. A. Schmeltzer, "Hollow metallic and dielectric waveguides for long distance optical transmission and lasers," Bell Syst. Tech. J. **43**(4), 1783–1809 (1964).

32. M. Miyagi, K. Harada, and S. Kawakami, "Wave propagation and attenuation in the general class of circular hollow waveguides with uniform curvature," IEEE Trans. Microwave Theory Tech. **32**(5), 513–521 (1984).

33. W.-H. Lee, "Binary computer-generated holograms," Appl. Opt. **18**(21), 3661–3669 (1979).

34. S. Turtaev, I. T. Leite, K. J. Mitchell, *et al.*, "Comparison of nematic liquid-crystal and dmd based spatial light modulation in complex photonics," Opt. Express **25**(24), 29874–29884 (2017).

35. B. Mastiani and I. M. Vellekoop, "Noise-tolerant wavefront shaping in a hadamard basis," Opt. Express **29**(11), 17534–17541 (2021).

36. E. Candes, J. Romberg, Caltech, *et al.*, "l1-magic: Recovery of sparse signals via convex programming," **4**, 16 (2005), www.acm.caltech.edu/l1magic/downloads/l1magic.pdf.

37. E. J. Candès, J. Romberg, and T. Tao, "Robust uncertainty principles: Exact signal reconstruction from highly incomplete frequency information," IEEE Trans. Inf. Theory **52**(2), 489–509 (2006).

38. C. Li, W. Yin, H. Jiang, *et al.*, "An efficient augmented lagrangian method with applications to total variation minimization," Comput. Optim. Appl. **56**(3), 507–530 (2013).